JOURNAL OF THEORETICAL AND APPLIED MECHANICS
62, 1, pp. 61-73, Warsaw 2024
https://doi.org/10.15632/jtam-pl/175498

RESEARCH ON VIBRATION CHARACTERISTICS OF MOTORIZED SPINDLE AT HIGH SPEED BASED ON POWER FLOW

Yudong Bao, Zhentao Zhou, Linkai Wu, Ye Dai

Key Laboratory of Advanced Processing Technology and Intelligent Manufacturing (Heilongjiang Province), Harbin University of Science and Technology, Harbin, China, and
School of Mechanical and Power Engineering, Harbin University of Science and Technology, Harbin, China
corresponding author Yudong Bao, e-mail: baoyudong@hrbust.edu.cn

To show dynamic properties of a motorized spindle at high speed, C01 type motorized spindle bearing-rotor system is used as a study object, and the dynamic model of the bearing-rotor system is established. The method to analyze vibration characteristics of motorized spindles by power flow is proposed, and it is found that the vibration energy is not necessarily considerable at the position where the vibration displacement response is significant. Finally, the system vibration energy distribution under different bearing stiffness is analyzed. The power flow method can analyze the dynamic characteristics of the bearing-rotor system in terms of energy distribution.

Keywords: harmonic response, motorized spindle, natural frequency, power flow, vibration characteristics

1. Introduction

As the core component of CNC machine center processing, the working performance of the motorized spindle will affect quality of processed parts. With the development of motorized spindles towards higher speed and higher precision, higher requirements are also placed on the dynamics of such systems. When the frequency of the external excitation reaches the natural frequency of the motorized spindle, the spindle system will resonate. Especially in high-speed and high-precision machining, the impact of the bearing-rotor system vibration characteristics on dynamic performance of motorized spindles cannot be neglected. For this reason, many scholars have conducted numerous researches on vibration characteristics of the bearing-rotor system.

Cao and Altintas (2007) put forward a general gauge model of the spindle system, which can simulate and analyze bearing performance, dynamic and static characteristics of the spindle. Shi *et al.* (2019) used MATLAB to obtain the natural frequency and critical speed of the motorized spindle, and analyzed the vibration response of the motorized spindle under the influence of unbalanced factors. Bai *et al.* (2018) established a vibration dynamics model of the broach--spindle-bearing dual rotor system under the condition of a high-speed cutting force on the spindle end, and carried out finite element analysis on the natural frequency and mode shape of the motorized spindle. Huang *et al.* (2016) established dynamics of the motorized spindle based on the finite element beam theory model, and obtained the vibration response of the motorized spindle under different rotational speeds, bearing clearance and initial eccentricity. Wang and Peng (2013) obtained the 1st to 5th order natural frequencies and mode shapes of the spindle with vibration modal analysis of the ceramic electro-spindle. Although the motorized spindle bearing-rotor system has a certain research foundation in terms of vibration characteristics, the vibration analysis of the system has not been thoroughly studied from the energy viewpoint.

The vibrating energy information from the shaft system can be reflected by the power flow analysis, and then the motorized spindle vibration characteristics can be described more accurately. Chen *et al.* (2013) established a high-speed motorized spindle power flow model based on the law of energy conservation, and simulated and analyzed the temperature rise of each part of the motorized spindle. Xiao (2021) used the power flow method to study the actual vibration state of the rolling mill. According to the analysis results, vibration suppression measures were taken, and a good vibration suppression effect was achieved. Rejab *et al.* (2014) studied the vibration power flow of the paddy power-train bracket of a passenger car, and obtained the main noise transmission path and resonance frequency. Qiao *et al.* (2016) used the power flow method combined with vibration energy to evaluate active vibration isolation performance of rotating machinery, and proposed an indirect measurement method related to power flow and vibration energy.

By analyzing the literature, it can be seen that the power flow method can be combined with data visualization means to visually describe the vibration energy distribution pattern and vibration transmission path in mechanical structures, which can be used as a reference for analyzing system characteristics or vibration isolation and suppression capability. The displacement response is usually a localized indicator of the structure, while the power flow response can provide global information. The power flow is very sensitive to changes in structural parameters and damage relative to the displacement response. By analyzing the path and distribution of the power flow, the load transfer mechanisms and energy flow paths within the structure can be better understood, and the energy of the vibration source entering the end of the spindle through different transfer paths can be reduced to increase the machining accuracy. Thus, it has great application and research space in analyzing system structural characteristics and fault and damage diagnosis.

Therefore, this paper introduces power flow in the study of motorized spindle vibration characteristics, takes C01 type motorized spindle bearing-rotor system as the research object. Then the first six-order natural frequencies and mode shapes of the motorized spindle are obtained by simulation, and the modal analysis test bench is set up to confirm correctness of the simulating results.

2. Mathematical model

2.1. Structural analysis of the motorized spindle

Motorized spindles primarily consist of bearings, motor, spindle, cooling system, tool changing system, sealing structure, etc. The motor, spindle and bearings are the core processing components of the motorized spindle. To analyze dynamic characteristics of the motorized spindle, the corresponding dynamic model needs to be established first (Gao *et al.*, 2020). Combined with the structure of the motorized spindle, the rotor of the motor is fixed on the main shaft to form the rotor part, and the two ends of the rotor are supported by bearings, which are a typical rotor support system. Therefore, the rotor dynamics theory is used to model the motorized spindle system.

The cross-sectional view and node division of C01 type motorized spindle is shown in Fig. 1. The part circled by the red frame in the figure is the rotating body of the motorized spindle, and it is also the bearing-rotor system simulated in this paper. The bearing-rotor system obtained after node division is divided into 23 nodes and 22 shaft elements. The properties of each beam element are defined based on length, diameter and material properties of the corresponding shaft elements, then rigid disc elements are superimposed at appropriate positions to represent the concentrated mass.

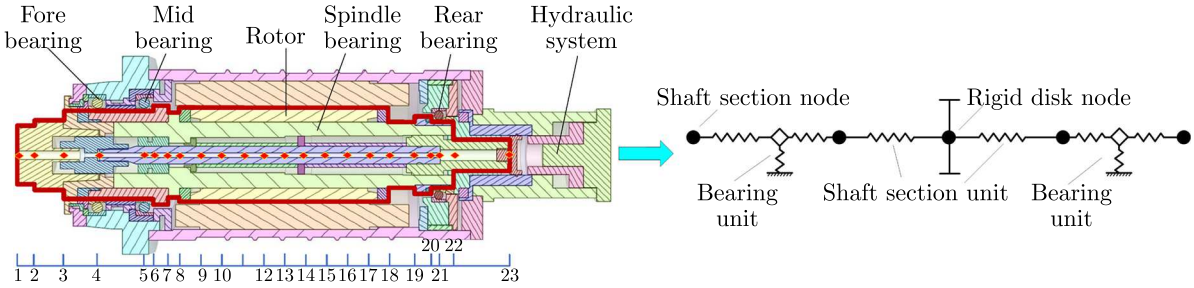

Fig. 1. Motorized spindle rotor system and the simplified model

2.2. Quasi-static model of the angular contact ball bearing

After the bearing is externally loaded, the relative position of the center of the rolling element and the curvature center of the inner and outer rings will change, as shown in Fig. 2.

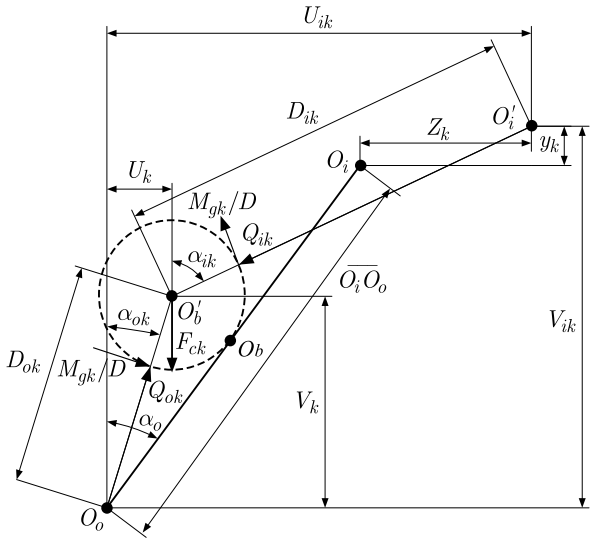

Fig. 2. Bearing inner ring curvature center change and the force diagram

The forces and torques exerted on the bearing ring (Yang *et al.*, 2022) are

$$F_{xi} = \sum_{k=1}^{N}\left(Q_{ik}\sin\alpha_{ik} + \frac{M_{gk}}{D}\cos\alpha_{ik}\right) \qquad F_{xo} = \sum_{k=1}^{N}\left(Q_{ok}\sin\alpha_{ok} + \frac{M_{gk}}{D}\cos\alpha_{ok}\right)$$

$$F_{yi} = \sum_{k=1}^{N}\left(Q_{ik}\cos\alpha_{ik} - \frac{M_{gk}}{D}\sin\alpha_{ik}\right)\cos\varphi_k$$

$$F_{yo} = \sum_{k=1}^{N}\left(-Q_{ok}\cos\alpha_{ok} - \frac{M_{gk}}{D}\sin\alpha_{ok}\right)\sin\varphi_k$$

$$F_{zi} = \sum_{k=1}^{N}\left(Q_{ik}\cos\alpha_{ik} - \frac{M_{gk}}{D}\sin\alpha_{ik}\right)\sin\varphi_k$$

$$F_{zo} = \sum_{k=1}^{N}\left(-Q_{ok}\cos\alpha_{ok} - \frac{M_{gk}}{D}\sin\alpha_{ok}\right)\sin\varphi_k \tag{2.1}$$

$$M_{yi} = \sum_{k=1}^{N}\left[r_{ic}\left(Q_{ik}\sin\alpha_{ik} + \frac{M_{gk}}{D}\cos\alpha_{ik}\right) - f_i M_{gk}\right]\sin\varphi_k$$

$$M_{yo} = \sum_{k=1}^{N}\Big[r_{oc}\Big(Q_{ok}\sin\alpha_{ok} + \frac{M_{gk}}{D}\cos\alpha_{ok}\Big) - f_o M_{gk}\Big]\sin\varphi_k$$

$$M_{zi} = -\sum_{k=1}^{N}\Big[r_{ic}\Big(Q_{ik}\sin\alpha_{ik} + \frac{M_{gk}}{D}\cos\alpha_{ik}\Big) - f_i M_{gk}\Big]\cos\varphi_k$$

$$M_{zo} = \sum_{k=1}^{N}\Big[r_{oc}\Big(Q_{ok}\sin\alpha_{ok} + \frac{M_{gk}}{D}\cos\alpha_{ok}\Big) - f_o M_{gk}\Big]\cos\varphi_k$$

where O_i, O_o and O_b represent the initial center of curvature of the inner and outer raceways of the bearing and the center of the rolling element, and refer to the center of the rolling element and the center of curvature of the inner ring raceway after the bearing is deformed by the force. U_{ik} and V_{ik} are the distance between the centers of curvature of the inner and outer ring raceways after loading, U_k and V_k represent the distance between the center of the rolling element and the curvature centers of the inner and outer ring raceways after loading, and the subscript k represents the k-th rolling element. α_0 is the initial contact angle of the bearing, α_{ik} and α_{ok} represent the contact angle of the inner and outer raceways after deformation under the load. The contact deformation n of the inner and outer ring is set as δ_{ik} and δ_{ok}, and rolling body diameter is expressed as D. Q_{ik} is the action force applied to the rolling element by the inner ring, and Q_{ok} is the force exerted on the rolling element by the outer ring. M_{gk} is the torque acting on the rolling element, and F_{ck} is the centrifugal force of the rolling element.

According to the geometric relationship, α_{ik} and α_{ok} can be represented by U_k and V_k

$$\begin{aligned} \sin\alpha_{ok} &= \frac{U_k}{(f_o-0.5)D+\delta_{ok}} & \cos\alpha_{ok} &= \frac{V_k}{(f_o-0.5)D+\delta_{ok}} \\ \sin\alpha_{ik} &= \frac{U_{ik}-U_k}{(f_i-0.5)D+\delta_{ik}} & \cos\alpha_{ik} &= \frac{V_{ik}-V_k}{(f_i-0.5)D+\delta_{ik}} \end{aligned} \tag{2.2}$$

The relationship between bearing the deformation and applied force can be expressed as

$$\mathbf{F} = \mathbf{K}\boldsymbol{\delta} \tag{2.3}$$

The stiffness matrix can be obtained by taking partial derivative of Eq. (2.3) with respect to the deformation $\boldsymbol{\delta} = [\delta_x, \delta_y, \delta_z, \gamma_y, \gamma_z]$

$$\mathbf{K} = \begin{bmatrix} \dfrac{\partial F_x}{\partial \delta_x} & \dfrac{\partial F_x}{\partial \delta_y} & \dfrac{\partial F_x}{\partial \delta_z} & \dfrac{\partial F_x}{\partial \gamma_y} & \dfrac{\partial F_x}{\partial \gamma_z} \\ \dfrac{\partial F_y}{\partial \delta_x} & \dfrac{\partial F_y}{\partial \delta_y} & \dfrac{\partial F_y}{\partial \delta_z} & \dfrac{\partial F_y}{\partial \gamma_y} & \dfrac{\partial F_y}{\partial \gamma_z} \\ \dfrac{\partial F_z}{\partial \delta_x} & \dfrac{\partial F_z}{\partial \delta_y} & \dfrac{\partial F_z}{\partial \delta_z} & \dfrac{\partial F_z}{\partial \gamma_y} & \dfrac{\partial F_z}{\partial \gamma_z} \\ \dfrac{\partial M_y}{\partial \delta_x} & \dfrac{\partial M_y}{\partial \delta_y} & \dfrac{\partial M_y}{\partial \delta_z} & \dfrac{\partial M_y}{\partial \gamma_y} & \dfrac{\partial M_y}{\partial \gamma_z} \\ \dfrac{\partial M_z}{\partial \delta_x} & \dfrac{\partial M_z}{\partial \delta_y} & \dfrac{\partial M_z}{\partial \delta_z} & \dfrac{\partial M_z}{\partial \gamma_y} & \dfrac{\partial M_z}{\partial \gamma_z} \end{bmatrix} \tag{2.4}$$

2.3. Kinematic model of the rigid disc element

The motorized spindle shaft system is simplified to a single-disc rotor system as shown in Fig. 3. $OXYZ$ is a fixed coordinate system, o is the center of the disc, Ω and is the shaft speed. The shaft AB bends in the rotating state, and the deformed axis is represented by $A'B'$. P is any point on the disc, its position angle is denoted by φ, and the distance from the center of the disc is r.

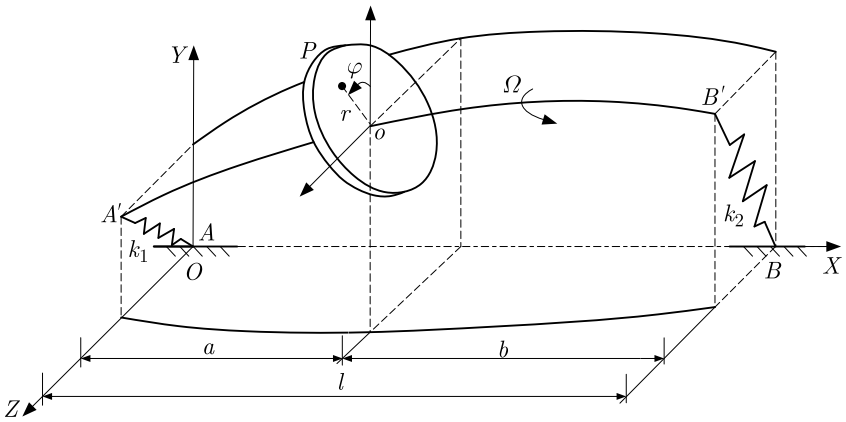

Fig. 3. Motorized spindle shaft system

The velocity of point P can be obtained by derivation

$$\begin{aligned}
\dot{x} &= \dot{u} + \Omega r\theta_z \sin\varphi + \Omega r\theta_y \cos\varphi - r\dot{\theta}_z \cos\varphi + r\dot{\theta}_y \sin\varphi \\
\dot{y} &= \dot{v} - \Omega r \sin\varphi - r\theta_z\dot{\theta}_z \cos\varphi \\
\dot{z} &= \dot{w} + \Omega r \cos\varphi - r\theta_y\dot{\theta}_y \sin\varphi
\end{aligned} \tag{2.5}$$

The total kinetic energy of the disc can be expressed as

$$T = \frac{1}{2}\int_b^a \int_0^{2\pi} l_d \rho r(x^2 + y^2 + z^2)\, dr\, d\varphi \tag{2.6}$$

where l_d is width of the disc, ρ is density, b is inner diameter of the disc, and a is the outer diameter.

Ignoring the effect of damping, the differential equation of motion for a rigid disc is

$$\mathbf{M}^d\ddot{\mathbf{q}} - \Omega\mathbf{G}^d\dot{\mathbf{q}} = \mathbf{F}^d \tag{2.7}$$

where $\mathbf{M}^d$ is the mass matrix of the disc, $\mathbf{G}^d$ is the gyro matrix, $\mathbf{F}^d$ is the external force vector, $\mathbf{q}$ is the displacement vector.

2.4. Elastic shaft element motion model

The Timoshenko beam element and its deformed structure are shown in Fig. 4 (Du and Liu, 2014). Each beam element has two left and right nodes A and B, and the node displacement is set as $\mathbf{q} = [u, v, w, \theta_y, \theta_z]^{\mathrm{T}}$.

The expression for kinetic energy of the beam element of length L is

$$T = \int_0^L \frac{1}{2} J\rho\Omega^2\, dz + \int_0^L \frac{1}{2}\rho A(\dot{u}^2 + \dot{v}^2 + \dot{w}^2)\, dz + \int_0^L \frac{1}{2} I\rho(\dot{\theta}_y^2 + \dot{\theta}_z^2)\, dx + \int_0^L \frac{1}{2}\Omega J\rho(\dot{\theta}_y\theta_z - \theta_y\dot{\theta}_z)\, dx \tag{2.8}$$

where I is radial moment of inertia, J is polar moment of inertia, and R is radius of the beam element section.

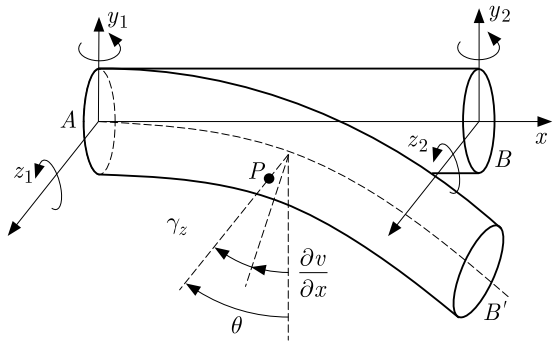

Fig. 4. Timoshenko beam and its deformation

The potential energy of the beam element is

$$\begin{aligned} V = &\int_0^L \frac{1}{2}EA\Big(\frac{\partial u}{\partial x}\Big)^2\,dx + \int_0^L \frac{1}{2}EI\Big[\Big(\frac{\partial \theta_y}{\partial x}\Big)^2 + \Big(\frac{\partial \theta_z}{\partial x}\Big)^2\Big]\,dx \\ &+ \int_0^L \frac{1}{2}k_sAG\Big[\Big(\theta_y + \frac{\partial w}{\partial x}\Big)^2 + \Big(\theta_z - \frac{\partial v}{\partial x}\Big)^2\Big]\,dx \\ &+ \int_0^L \frac{1}{2}EA\left[\left(\frac{1}{2}\Big(\frac{\partial v}{\partial x}\Big)^2\right)^2 + \left(\frac{1}{2}\Big(\frac{\partial w}{\partial x}\Big)^2\right)^2\right]dx \end{aligned} \tag{2.9}$$

The work done by the external force is

$$W = \int_0^L (q_x u + q_y v + q_z w + m_y\theta_y + m_z\theta_z)\,dx + \int_0^L \frac{1}{2}\Omega^2 v^2\rho A\,dx + \int_0^L \frac{1}{2}\Omega^2 w^2\rho A\,dx \tag{2.10}$$

Combined with the generalized Hamilton principle

$$\delta I = \delta\int_{t_1}^{t_2}(T - V + W)\,dt = 0 \tag{2.11}$$

The differential equation of beam motion in matrix form is

$$\mathbf{F}^b = \mathbf{M}^b\ddot{\mathbf{q}} - \Omega\mathbf{G}^b\dot{\mathbf{q}} + (\mathbf{K}^b - \Omega^2\mathbf{M}_C^b)\mathbf{q} \tag{2.12}$$

where $\mathbf{M}^b$ is the mass matrix of the beam, $\mathbf{M}_C^b$ is the mass matrix used to calculate the centrifugal force, $\mathbf{G}^b$ is the gyro matrix considering the gyro effect, $\mathbf{K}^b$ is the stiffness matrix, and $\mathbf{F}^b$ is the force vector.

Combining the differential equations of motion of the bearing model, rigid disc and beam elements, the differential equation of motion of the bearing-rotor system can be expressed as

$$\mathbf{M}_{sys}\ddot{\mathbf{q}} - \mathbf{D}_{sysy}\dot{\mathbf{q}} + \mathbf{K}_{sys}\mathbf{q} = \mathbf{F}_{ext} \tag{2.13}$$

where $\mathbf{M}_{sys}$ is the mass matrix of the system, $\mathbf{D}_{sys}$ is the system damping matrix (including the gyro matrix), $\mathbf{K}_{sys}$ is the system stiffness matrix, $\mathbf{q}$ and $\mathbf{F}_{ext}$ is the displacement vector and the external excitation force, respectively.

2.5. Power flow theory of the bearing-rotor system

The propagation of vibration in the mechanical structure is actually the propagation of vibration energy. The theoretical idea of the vibration power flow is to use the energy angle to describe the vibration propagation in the system. By introducing the power flow concept, both the magnitude for the force and speed and their phase relationship are considered, which avoids some problems caused by simply using the effective value of speed or acceleration to express the difference in the vibration level (Liu *et al.*, 2010; Li and Wu, 2015).

Assume $F(t)$ is the force acting on a node of the structure at a certain time, and $V(t)$ is the node velocity due to excitation. The time-domain expression of the vibration power flow is

$$P(t) = F(t)V(t) \tag{2.14}$$

Because the power flow at each node varies over time, the average power flow over a while is calculated in the frequency domain. Then, the corresponding power flow calculation expression is as follows

$$P = \frac{1}{T}\lim_{T\to\infty}\int_0^T F(t)V(t)\,dt \tag{2.15}$$

For a simple harmonic excitation $F = |F|\cos(\omega t)$, the system will produce a simple harmonic motion with the same frequency as the excitation force but lagged by a phase angle φ. The response of the system is superimposed by the instantaneous response and the steady-state response. The former will disappear owing to the damping loss within a period of time. The steady-state power flow can be expressed as

$$\begin{aligned} P &= \frac{1}{T}\int_0^T FV\,dt = -\frac{1}{T}\int_0^T |F|\cos(\omega t)\omega|X|\sin(\omega t+\varphi)\,dt \\ &= -\frac{\omega}{2}|F|\,|X|\sin\varphi = -\pi f|F|\,|Xt|\sin\varphi \end{aligned} \tag{2.16}$$

where ω is the angular velocity, t is time, φ is the phase angle, and $|X|$ is the nodal displacement.

The power flow in complex representation is as follows

$$P = \frac{1}{T}\int_0^T \mathrm{Re}\,(\widetilde{F}\mathrm{e}^{\mathrm{i}\omega t})\,\mathrm{Re}\,(\widetilde{V}\mathrm{e}^{\mathrm{i}\omega t})\,dt = \frac{1}{2}\,\mathrm{Re}\,(FV^*) \tag{2.17}$$

where $\widetilde{F}$, $\widetilde{V}$ are all complex numbers, $(\cdot)^*$ means the conjugate, Re means the real part.

3. Results and discussion

3.1. Numerical simulation and experimental validation

The design rated speed of C01 motorized spindle is 20000 r/min, the material of the spindle is Copper Alloy, the material of the motor rotor is 20CrMnTi, and the material of the stator is Ni3H4. Table 1 shows the specific material parameters. The bearing preload settings of C01 motorized spindle are shown in Table 2.

The eigenvalues and eigenvectors of the system can be obtained numerically by solving Eq. (2.13). The eigenvalues correspond to natural frequencies, and the eigenvectors correspond to principal vibration patterns of the spindle bearing-rotor system, as shown in Fig. 5 and Table 3.

Table 1. Specific material properties

Material name	Density [kg/m^3]	Young's modulus [GPa]	Poisson's ratio
Copper alloy	8300	110	0.34
20CrMnTi	7800	207	0.25
Ni3H4	3440	304	0.24

Table 2. Prestressing force of each bearing specific material properties

Bearing	Front bearing	Middle bearing	Rear bearing
Preload [N]	1400	800	600

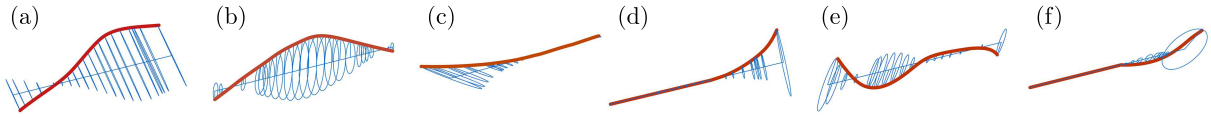

Fig. 5. Natural vibration mode of the rotor: (a) first order, (b) second order, (c) third order, (d) fourth order, (e) fifth order, (f) sixth order

Table 3. First six orders of the natural frequency [Hz] and vibration modes of spindle

Order	1	2	3	4	5	6
Frequency [Hz]	428.32	498.59	1621.6	2382.1	3697.3	5354.4
Mode shape	bending	bending	swing	swing	bending	swing

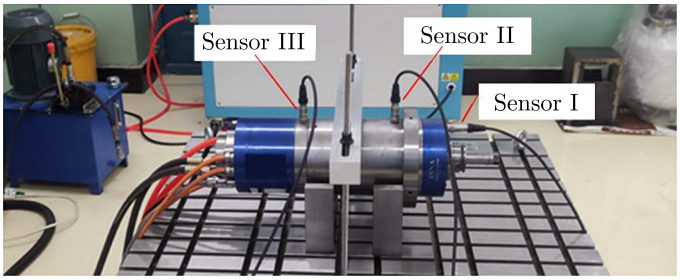

Fig. 6. Actual installation of vibration sensor

In order to obtain the natural frequency of C01 type motorized spindle, a modal experiment for the motorized spindle is designed. The basic principle of the modal experiment is: the motorized spindle placed on the V-shaped block is tapped with an impact hammer to excite the whole structure and make it vibrate, and the vibration response of different measuring points is collected by the acceleration sensor set on the outer shell of the motorized spindle. After the collected signal is sent to the dynamic signal analyzer for fast Fourier transform and other related analyses, the natural frequency of each order can be obtained.

As shown in Fig. 6, the three sensors are used for data acquisition in the modal experiment. Sensor I is arranged on the front bearing housing end face of the motorized spindle, and is used to measure axial vibration of the system. Sensors II and III are arranged at the front and rear ends of the outer housing corresponding to the bearing positions, and are used to measure radial vibration transmitted to the outer case through the bearings.

The frequency responding profiles of the three vibration measuring spots finally collected in the experiment are shown in Fig. 7. The first three natural frequencies of the modal experiment can be obtained as 115 Hz, 426 Hz, and 492 Hz, respectively. 426 Hz and 492 Hz correspond to the first two natural frequencies of 428.32 Hz and 498.59 Hz calculated from the simulation results. The mode shape of the smallest natural frequency measured in the experiment is axial torsion

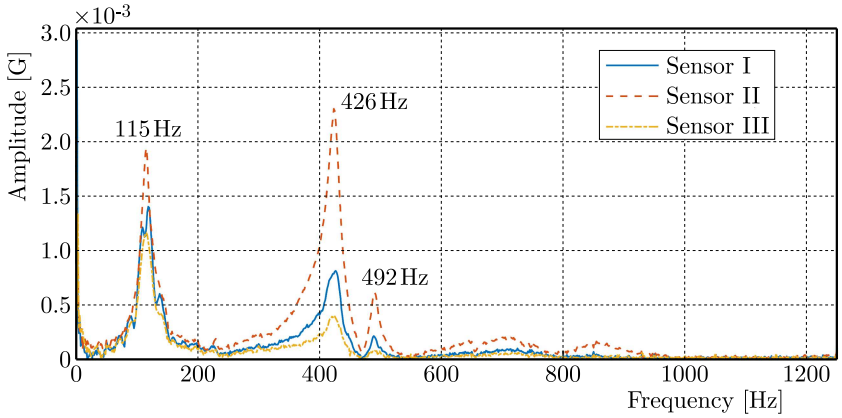

Fig. 7. Modal test results

(Chen *et al.*, 2014; Guo and Wu, 2006). Due to simplification of the model, the system stiffness becomes larger during superposition of the stiffness matrix, resulting in suppression of this frequency experimentally determined in the numerical simulation. The difference between the experimentally measured natural frequency and the simulated natural frequency is tiny, and the maximum error does not exceed 1.34%, which validates the accuracy of the theoretical modeling.

3.2. Comparison of the harmonic response power flow analysis under a mass unbalance excitation

The centrifugal force induced by mass eccentricity is one of the primary excitation sources. Through analysis of the harmonic response under the unbalanced excitation, the amplitude of the shaft system under eccentric mass action can be known, so as to judge whether the design of the spindle structure is satisfying for processing requirements.

Assuming that there is an eccentric mass on a disc, the resulting centrifugal force is

$$F = me\omega \tag{3.1}$$

where m is eccentric mass, e is the eccentricity radius, and ω is the rotation speed. F can be decomposed into two mutually perpendicular harmonic forces on the y and z axes

$$F_y = me\omega^2 \cos(\omega t) \qquad F_z = me\omega^2 \sin(\omega t) \tag{3.2}$$

Combined with the bearing-rotor dynamical model, the unbalanced mass point is set at the turntable, the offset distance is set to $0.1 \cdot 10^{-4}$ m, the analysis frequency range is 100-3000 Hz, and the damping of 0.008 Ns/mm is applied at the spring of the simulated bearing. The harmonic response analysis is performed and the displacement responses of each node of motorized spindle bearing-rotor system are displayed in Fig. 8.

Under the unbalanced excitation, the response peaks appear at each order natural frequency. The resonance amplitude of the second-order natural frequency is relatively small, indicating that the motorized spindle is not very sensitive to this order natural frequency under the unbalanced excitation. The response amplitude before the first-order natural frequency has been rising, indicating that the rigidity of the motorized spindle gradually decreases in this stage. The stiffness performance of the front end of the spindle is better than that of the middle and rear sections below 1500 Hz. After 1500 Hz, the front-to-back performance of the spindle is almost identical without a resonance, and the spindle back-end response value is smaller in the case of the resonance.

Figure 9 shows the power flow variation at each node of the rotor system with the frequency under the unbalanced excitation. The power flow response of the bearing-rotor system also

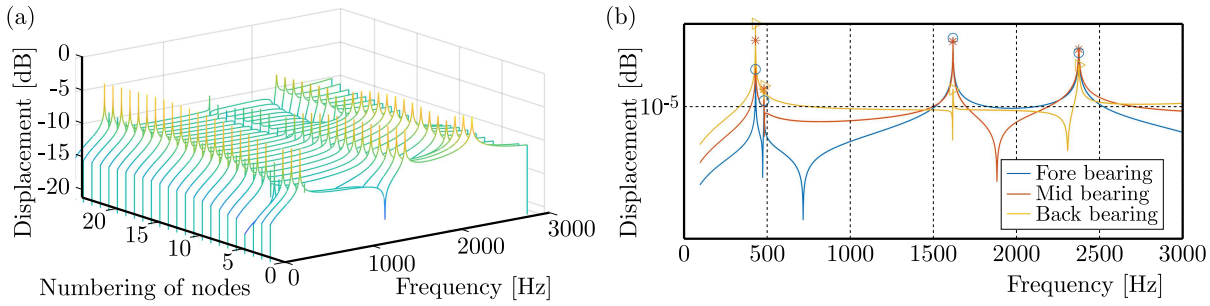

Fig. 8. Displacement response under the unbalanced mass excitation: (a) full node, (b) bearing nodes

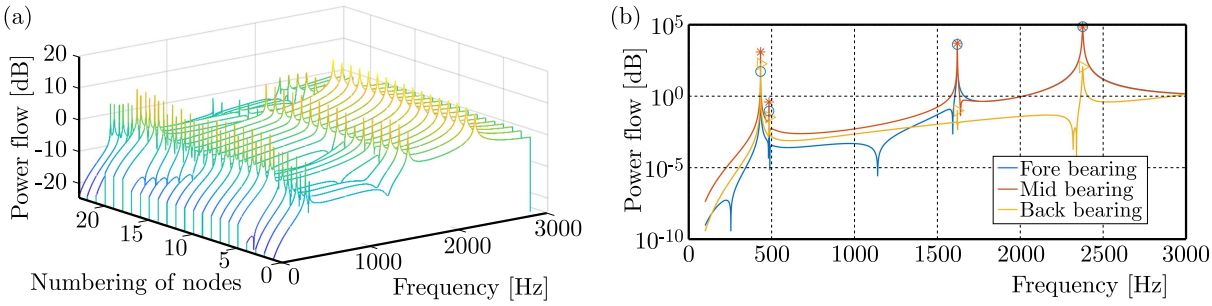

Fig. 9. Power flow of the rotor system: (a) full node, (b) bearing nodes

has resonance peaks at various natural frequencies. This is because the system will vibrate substantially under the resonance condition, and the vibration energy at this time should also have a maximum value. On the whole, the power flow response curve and the displacement response curve have similar fluctuation trends, which shows that the power flow method can analyze the dynamic impact of the bearing-rotor system from the perspective of energy. By comparing the power flow of the three bearing positions, it can be seen that under the unbalanced excitation, the power flow response of the front bearing in the frequency range of 100-1600 Hz is relatively low, and the power flow response of the front bearing is basically the same as that of the middle bearing after the third order natural frequency. Combined with the displacement response under the unbalanced excitation, at the first two orders of natural frequency, the displacement response of the rear bearing is the largest, but the power flow response is close to or less than that at the front and middle bearings. On the whole, the power flow response curves of the front and intermediate bearings are closer to the displacement response. These phenomena show that in terms of power flow, the energy at the rear bearing is relatively small, and the energy distribution of the front and middle bearings is close due to their close positions, which reflects the difference between power flow analysis and harmonic response analysis.

3.3. Effect of bearing stiffness on the system power flow

The power flow analysis method is very sensitive to structural or parameter changes of the system, so different bearing stiffnesses are set, and the corresponding power flow response curves are calculated to analyze the effect that bearing support rigidity has over the system dynamic characteristics.

For the spindle bearing support structure, only one bearing support stiffness is changed at a time. In order to make the simulation results optimal and not distorted, the bearing stiffness change amplitude is set to 0.3 K, and the radial stiffness of the front, middle and rear bearings are $3.5 \cdot 10^8$ N/mm (K_1), $2.6 \cdot 10^8$ N/mm (K_2) and $1.9 \cdot 10^8$ N/mm (K_3). Under working condition 1, only the stiffness of the front bearing K_1 is changed, under case 2, only the stiffness of the front bearing is changed K_2, and so on, totaling 9 different support conditions. The power flow

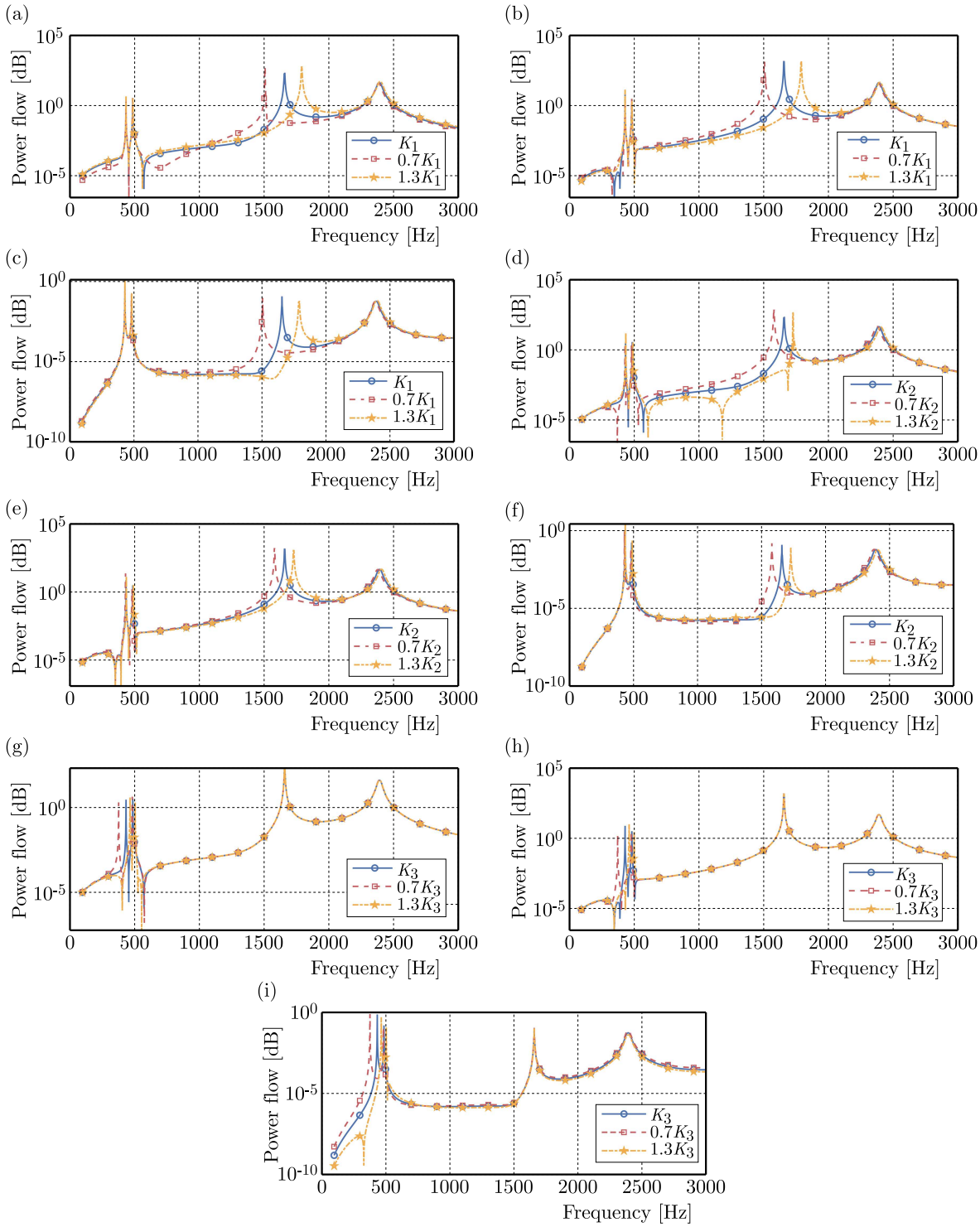

Fig. 10. Power flow response of each bearing position under different working conditions

curves under each working condition are given in Fig. 10. Changing the front bearing support stiffness has the greatest effect on the 3rd order natural frequency, which shows that the 3rd order natural frequency decreases when the front bearing support stiffness decreases, and the other order natural frequencies remain approximately the same. Increasing the mid-bearing support stiffness causes a large increase in the 3rd-order natural frequency and a small increase in the 4th-order natural frequency. Raising the rigidity of the intermediate bearing has almost no impact on the power flow at the middle bearing position, but causes a large increase in the

power flow at the front bearing position within 500 Hz to 1600 Hz. Changing the rear bearing stiffness mainly affects the 1st and 2nd order natural frequencies, and has basically no effect on the region above 1000 Hz. An increase in the rear bearing stiffness enlarges the 1st and 2nd order natural frequencies, making the 1st and 2nd order resonance peak distances smaller, which helps the system to quickly jump over the resonance region.

In summary, the power flow analysis can further analyze dynamic characteristics of motorized spindles from the energy point of view. The changes in the system structure or parameters are reflected in the power flow response, indicating that power flow analysis methods can be applied to analyze structure changes and guide structural optimization or fault detection work.

4. Conclusion

In this paper, the harmonic response and power flow of the bearing-rotor system are studied by establishing the bearing-rotor dynamic model of the motorized spindle, and the displacement response and energy distribution of the system nodes are obtained and compared. The main conclusions are as follows:

- The first six natural frequencies of the bearing-rotor system are acquired through finite element simulation, and the first three natural frequencies have large fluctuations, which are 428.32 Hz, 498.59 Hz, and 1621.6 Hz, respectively. Despite the failure to obtain the natural frequency at low rotational speeds, the largest error between simulation results and high-speed range experimental results does not exceed 1.34%.
- The method of analyzing the vibration characteristics of the motorized spindle bearing--rotor system at high speeds by the power flow is proposed. The displacement response at the rear bearing is the largest at the first two orders of natural frequency, but its power flow response is close to or smaller than the power flow response at the front and middle bearings.
- The bearing stiffness change has a greater influence on the first 3 orders of natural frequency of the system, and stiffness changes of the front and middle bearings mainly affect the position of the vibration power flow peak at the 3rd order of natural frequency. The rear bearing stiffness changes mainly affect the position of the peak of the vibration power flow at the 1st and 2nd order natural frequency.

Acknowledgments

This work has been supported by Opening Project of the Key Laboratory of Advanced Processing Technology and Intelligent Manufacturing (Heilongjiang Province), Harbin University of Science and Technology (KFKT202205), and National Natural Science Foundation of China (51875142), China.

References

1. Bai X.J., Li J.Y., Gou W.D., 2018, Vibration analysis and research of high speed motorized spindle under the influence of cutting force, *Journal of Qinghai University*, **36**, 1, 61-69+74
2. Cao Y.Z., Altintas Y., 2007, Modeling of spindle-bearing and machine tool systems for virtual simulation of milling operations, *International Journal of Machine Tools and Manufacture*, **47**, 9, 1342-1350
3. Chen X.A., Zhang P., He Y., 2013, Power flow model of high-speed motorized spindles and its thermal characteristics, *Transactions of the Chinese Society for Agricultural Machinery*, **44**, 9, 250-254
4. Chen X.A., Zhang P., He Y., 2014, Axial vibration of high-speed motorized spindles, *Journal of Vibration and Shock*, **33**, 20, 70-74+90

5. Du L.H., Liu F.K., 2014, Analysis of beam deflection based on euler and Timoshenko theory, *Journal of Lanzhou Institute of Technology*, **21**, 2, 41-44
6. Gao F., Cheng M.K., Li Y., 2020, Analysis of coupled vibration characteristics of PMS grinding motorized spindle, *Journal of Mechanical Science and Technology*, **34**, 9, 3497-3515
7. Guo D.Q., Wu Y.H., 2006, The model analysis of the ceramic bearing electric spindle, *Development and Innovation of Machinery and Electrical Products*, **19**, 1, 7-8
8. Huang W.D., Gan C.B., Yang S.X., 2016, Dynamic modeling and vibration response analysis of high speed motorized spindle, *Journal of Zhejiang University (Engineering Science)*, **50**, 11, 2198-2206
9. Li G., Wu W.W., 2015, Vibration and sound radiation research based on power flow method, *Journal of Ship Mechanics*, **19**, 5, 609-618
10. Liu C.F., Zhang C., Zhang G.X., 2010, Dynamic stiffness analysis of DVG850 high-speed vertical machining center headstock, *Coal Mine Machinery*, **31**, 12, 88-90
11. Qiao B., Zhao T., Chen X., Liu J., 2016, The assessment of active vibration isolation performance of rotating machinery using power flow and vibrational energy: experimental investigation, *Proceedings of the Institution of Mechanical Engineers, Part C: Journal of Mechanical Engineering Science*, **230**, 2, 159-173
12. Rejab M.N.A., Rahman R.A., Hamzah R.I.R., 2014, Measurement of vibration power flow through elastomeric powertrain mounts in passenger car, *Applied Mechanics and Materials*, **471**, 30-34
13. Shi H.T., Zhao J.Z., Zhang Y., 2019, Dynamic modeling and vibration response analysis of 170SD30 ceramic motorized spindle, *Modular Machine Tool and Automatic Manufacturing Technique*, **542**, 4, 32-36+40
14. Wang W.K., Peng Y.Y., 2013, Ceramic motorized spindle vibration modal analysis based on ANSYS, *Electron Test*, **8**, 136-138
15. Xiao B., 2021, *Research on Vibration Energy of Hot Tandem Mill Based on Power Flow*, Dissertation. University of Science and Technology Beijing
16. Yang J.F., Shi Z., He Z.K., 2022, Theoretical model and simulation of the dynamic stiffness of angular contact ball bearing based on the analytical matrix method, *China Measurement and Test*, **48**, z1, 129-134

Manuscript received June 19, 2023; accepted for print August 28, 2023